ADVANCED FUNCTIONAL MATERIALS
www.afm-journal.de

In Operando Near-Field Optical Investigation of Memristive Ta_2O_5 Thin Film Devices with a Graphene Top Electrode

Konstantin G. Wirth, Kalle Goss, Thomas Heisig, Christoph Bauerschmidt, Andreas Hessler, Haolong Li, Lutz Waldecker, Regina Dittmann, and Thomas Taubner**

Resistive switching devices based on metal oxides are candidates for nonvolatile memory storage. They often rely on the valence change mechanism, the field-induced movement of donor ions leading to nanoscale conductive paths in filamentary-type devices. Devices usually consist of a transition metal oxide like Ta_2O_5 sandwiched between two metal electrodes. Critical parameters of the devices, such as cycle-to-cycle variability, R_{off}/R_{on} ratio, and endurance depend on the morphology and composition of the filaments. However, investigating filaments on the nanoscale is cumbersome, and commonly applied techniques such as conductive atomic force or transmission electron microscopy require delaminating the metal top electrode, inhibiting in operando investigations over many switching cycles. Here, the authors use infrared scattering-type scanning near-field optical microscopy (s-SNOM) to investigate resistive switching in Ta_2O_5 films with a graphene top electrode in operando and reveal individual filaments on the device level. By selecting an appropriate illumination frequency, the authors can trace the evolution of filaments and the joule heating-induced retraction of the top electrode until device failure. s-SNOM promises a deeper understanding of resistive switching devices' microscopic switching behavior and applies to a wide range of resistive switching oxides, such as HfO_2, $SrTiO_3$, and SiO_2.

1. Introduction

Resistive switching memory devices, or resistive random-access memories (ReRAM), are prime candidates for non-volatile memory applications due to low power consumption, nanosecond response time, and excellent retention.[1,2] For storing information, ReRAMs utilize the resistance difference between a high-Ohmic (MΩ or GΩ) state and a low-Ohmic (Ω or kΩ) state, which can be reversibly switched. Transition metal oxides (TMO) such as $SrTiO_3$, HfO_2, and Ta_2O_5 are promising materials for realizing ReRAMs, with Ta_2O_5 being of technological relevance due to its compatibility with complementary metal-oxide-semiconductor technology,[3] ease of fabrication, and high cyclability.[4] ReRAM devices typically consist of a TMO sandwiched between two electrodes, one with a low work function metal that leads to an ohmic contact to the oxide, and another inert electrode with a high work function resulting in a Schottky barrier at the oxide interface.[5,6]

The valence change mechanism (VCM) is commonly employed to explain resistive switching in Ta_2O_5-based ReRAMs, where applying an electric field leads to the formation, migration, and accumulation of oxygen vacancies, creating conductive filaments.[7,8] Filament position, morphology, geometry, and composition significantly influence device-level characteristics such as device-to-device, cycle-to-cycle variability, and endurance.[9,10] Filament diameters in the devices can vary depending on the material, for example, for Ta_2O_5, the reported filament diameter ranges from 10 to 100 nm.[7,11–13] With decreasing diameter, the investigation of the filaments becomes more challenging. Electron-based imaging techniques such as transmission electron microscopy (TEM),[12] provide angstrom resolution, but require complex or destructive sample preparation procedures. Among scanning probe techniques conductive atomic force microscopy (c-AFM),[14] scanning tunneling microscopy (STM),[15] and scanning thermal microscopy (SThM)[16,17] have been used to study filaments. In c-AFM, a filament can be visualized by its higher conductivity compared to its surroundings. Tomographic imaging of the programmed device is possible by reconstructing the 3D structure from the current images with nanometric resolution, by ablating the filament layer

K. G. Wirth, C. Bauerschmidt, A. Hessler, H. Li, T. Taubner
1st Institute of Physics (IA) and JARA-FIT
RWTH Aachen University
52074 Aachen, Germany
E-mail: wirth@physik.rwth-aachen.de; taubner@physik.rwth-aachen.de
K. Goss, T. Heisig, R. Dittmann
Peter Gruenberg Institute – Electronic Materials (PGI-7) and JARA-FIT
Forschungszentrum Juelich GmbH
52425 Juelich, Germany
L. Waldecker
2nd Institute of Physics and JARA-FIT
RWTH Aachen University
52074 Aachen, Germany

The ORCID identification number(s) for the author(s) of this article can be found under https://doi.org/10.1002/adfm.202312980

DOI: 10.1002/adfm.202312980

by layer.[18] This provides unique insight into the shape of a filament and reveals the relation between current, filament size,[18] and growth.[19] For surface-sensitive techniques such as c-AFM and STM, investigations can only be performed after the delamination of the top electrode layer. Thus, the devices cannot be further switched after the measurements, which prevents the observation of the filament's evolution.

SThM enables nanoscale temperature measurements of hot spots at filaments in ReRAM devices, even through a top electrode layer. These measurements revealed differences in the heat dissipation between different top electrode materials such as TiN, Au, or graphene.[16,17] The limitation of SThM comes in the visualization of filaments with low local joule heating, such as filaments in the high resistive-low current state (HRS). For a detailed summary of memristive switches' in situ characterization techniques, refer to Sun et al.[20]

Another approach to characterize filaments is to use photoelectric effect-based techniques such as X-ray photoemission electron microscopy (XPEEM), which is sensitive to elements and valence states. XPEEM revealed in Ta_2O_5 devices the switching mechanism based on the generation of oxygen vacancies and revealed the O/Ta ratio in an individual filament of 2 ± 0.1.[13] However, XPEEM requires a synchrotron source and high-energy photons with high intensity. This can lead to damage to the sample. To study resistive switching in operando using XPEEM, instead of delaminating the metal top electrode, it can be replaced by graphene, which is transparent for photoelectrons.[13,21]

Optical far-field techniques are non-invasive but are limited by diffraction, making it challenging to study small structures such as filaments or requiring specialized analysis techniques such as contacting individual nanoparticles and leveraging their resonance shift.[22] Scattering-type scanning near-field optical microscopy (s-SNOM) overcomes the diffraction limit. s-SNOM uses locally enhanced near-fields (NF) at a sharp tip to optically record samples' properties in the scattered far-field light. It is a wavelength-independent technique and sensitive to the same excitation as far infrared spectroscopy,[23] making it suitable for studying the electronic and phononic properties of oxides. s-SNOM has been used to image structural information, charge carrier densities, and plasmon-phonon coupling in $SrTiO_3$ ceramics,[24–26] and imaging of a large (diameter > 500 nm) locally formed filament in $SrTiO_3$ was achieved.[24] Since the optical NF decays exponentially away from the tip and penetrates into the sample, s-SNOM offers non-destructive, subsurface imaging capability with a resolution down to 20 nm[27] and probing depths of up to 100 nm.[28] The probing depth depends on the vertical sample composition and the experimentally controllable effective decay length of the NF.[29] This should enable the characterization of filament morphology via imaging through a transparent electrode and the composition via nanospectroscopy. However, the application to TMO-based ReRAM devices and investigation of much smaller filaments in Ta_2O_5 have not yet been performed.

Investigating filaments in devices is even more challenging than analyzing locally switched filaments because the forming position is unknown a priori, such that the entire area of the top electrode needs to be scanned. These measurements also require a high spatial resolution and sufficient speed to overcome possible retention of a filament, and the method needs to be sensitive to excitation that allows for tracking of changes in the device over at least one switching step. Here, we investigate the morphology and composition of filaments in Ta_2O_5 thin films using amplitude and phase-resolved infrared s-SNOM. We start with imaging a locally switched Ta_2O_5 film without a top electrode and estimate the filament's composition by subsequent nanospectroscopy and theoretical modeling of the s-SNOM response. Furthermore, we show that ReRAM devices with graphene top electrode, in the same configuration as used for (X)PEEM, can be imaged in s-SNOM, and the morphology of the filaments can be tracked in operando in these devices below the top electrode. Thus allowing for switching and subsequent imaging of the device for up to seven switching steps to trace the filaments. Combining the s-SNOM data with *I–V* measurements of the device, we reveal that significant changes in the device morphology still lead to similar switching behavior. Finally, we reveal a failure reason for the specific device layout used here, namely the retraction of the graphene top electrode. These findings provide a basis for studying the structural changes in resistive switching materials and memristive devices with infrared light in s-SNOM.

2. Results

Imaging of switched filaments in Ta_2O_5 is challenging and requires high spatial resolution, as they appear stochastically in devices and are usually only up to 100 nm in diameter. Thus, we first conducted a proof-of-principle experiment to verify the imaging of filaments in Ta_2O_5 with s-SNOM. The filament was locally formed by placing a micrometer-sized tungsten tip mounted on a microcontroller on the 8 nm thick Ta_2O_5 thin film and applying a voltage with a current compliance of 200 µA (**Figure 1a**). Figure 1b shows the recorded *I–V* curve of the forming process. The *I–V* curve shows a sharp increase in current by multiple orders of magnitude at −6 V, characteristic of a forming step.

In Figure 1c, a schematic of the s-SNOM scan of the 8 nm Ta_2O_5 film on top of the Ta 30 nm thick bottom electrode, which serves as a back gate on top of the Si_3N_4 substrate, is shown. The s-SNOM's metalized tip is operated in tapping mode at a frequency Ω. S-SNOM records the optical near-field scattering amplitude (S_3) and phase (ϕ_3) at a specific laser wavelength by lock-in detection of the light scattered from an AFM tip at higher harmonics of the tip oscillation frequency. The amplitude and phase of the scattered light can be accessed with the help of the pseudo-heterodyne phase modulation.[30] The amplitude and phase of the scattered light are related to the complex permittivity $\epsilon(\nu)$ of the sample.

The s-SNOM's AFM topography and optical amplitude contrast (S_3) images recorded at 1200 cm^{-1} of the formed spot are shown in Figure 1d,e. Additional markers based on topographic features are set in white to compare the image to a local current measurement shown in Figure 1f; for details, see Section S1, Supporting Information. In the AFM topography image in Figure 1d, several inhomogeneities in the Ta_2O_5 film are present, but no hints of a filament can be observed. The amplitude contrast image in Figure 1e reveals a bright spot in the middle and weaker amplitude contrast in the surrounding regions, with some of the inhomogeneities observed in the AFM image resulting in a darker contrast compared to the surrounding film. Figure 1f shows a current image recorded with a conductive-AFM (c-AFM)

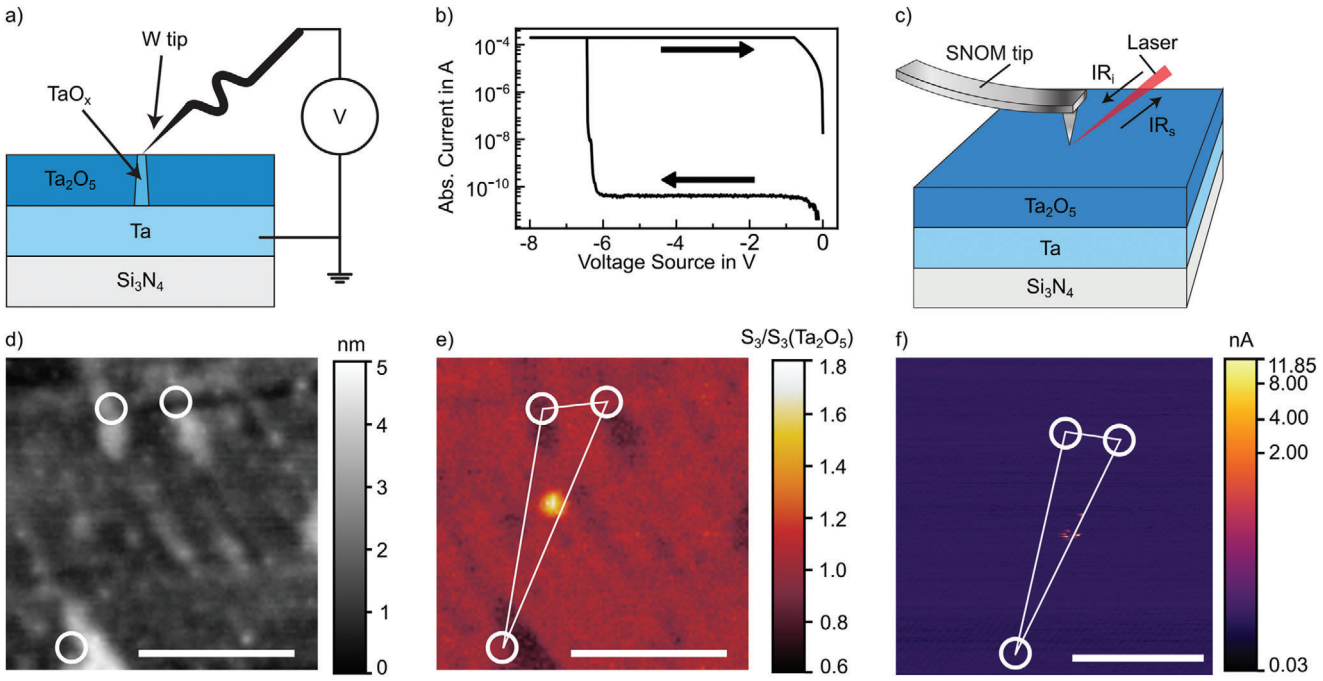

Figure 1. Proof of principle – identification of a locally formed filament in a Ta_2O_5 film. a) Schematic of the local forming of a filament in an 8 nm thick Ta_2O_5 film with a tungsten tip. The bottom Tantalum (Ta) electrode has a thickness of 30 nm. The substrate consists of Si_3N_4. b) *I–V* curve of the forming process, showing the characteristic jump in the current over orders of magnitude up to the current compliance of 200 µA upon filament formation. Black arrows mark the voltage sweep direction. c) Schematic of an s-SNOM measurement of the Ta_2O_5 thin film. The s-SNOM measurement was conducted after forming the filament. d) AFM and e) s-SNOM amplitude image (S_3) of the switched area recorded at 1200 cm^{-1}. The amplitude image reveals a bright spot. f) Conductive AFM (c-AFM) current image of the same area (slightly shifted and rotated), recorded after the s-SNOM measurements, shows spots of high current. An image with a logarithmic color scale can be found in SI S1. The markers in (d–f) highlight the position of the spots due to a slight rotation between s-SNOM and c-AFM measurements. The scale bars correspond to 500 nm.

at the same position as the s-SNOM measurements. The color scale of the image is non-linear because the current difference in the image is three orders of magnitude. The sample was slightly rotated as two different setups were used for s-SNOM and c-AFM measurements. Thus, the white markers are based on the same topographic features and are used to compare the images (triangulation shown in Figure S1, Supporting Information). The current image shows currents as small as 0.03 nA for the surrounding Ta_2O_5 film. In contrast, at a position corresponding to the bright spot in Figure 1d, a current of up to 11.85 nA is measured. These findings prove that the bright spot in the s-SNOM measurements is conductive and thus a filament. Therefore, s-SNOM microscopy can give insights into the filament's morphology, namely its position. The lateral diameter of the bright spot is 60 ± 5 nm (FWHM of the spot) based on s-SNOM scans, which is in good agreement with literature values for filaments in Ta_2O_5 of 10–100 nm.[7,11–13,31] Indicating the formation of a single filament. Generally, the lateral resolution in s-SNOM is limited to the radius of the metal-coated AFM tip, which is usually around 20 nm.[23,27] A detailed comparison of the resolution of s-SNOM and c-AFM can be found in Section S1, Supporting Information.

Next, we conduct s-SNOM spectroscopy of the filament to gain insights into its composition. We compare our results to permittivities of sputtered oxygen-deficient Ta_2O_x films with $x < 5$. (**Figure 2**). Details of the growth and stoichiometry analysis by X-ray photoelectron spectroscopy can be extracted from ref.[13] To obtain the permittivities of Ta_2O_5 and sub-stochiometric Ta_2O_x films, first, we recorded angle-dependent reflectance spectra of sputtered thin films with FTIR (see Experimental Section) and subsequently fitted the data. The permittivity of amorphous Ta_2O_5 can be described by a superposition of phonon modes (Lorentz oscillator) and free charge carrier contributions (Drude term).[32,33]

$$\varepsilon\ (\omega) = \varepsilon_1\ + i\,\varepsilon_2 = \varepsilon_\infty\ - \frac{\omega_p^2}{\omega^2 + i\gamma_D\omega} + \sum_{j=1}^{N} \frac{\omega_j^2}{\omega TO,j^2 - \omega^2 - i\Gamma_j\omega} \qquad (1)$$

where ϵ_∞ represents the contributions from higher frequencies. The free charge carrier contributions are characterized by the plasma frequency ω_p, and electronic damping γ_D. The phonon contributions are characterized by ω_j the phonon oscillator strength, $\omega_{,j}$ the resonance frequency, and Γ_j the width of the phonon resonance. We find that the dielectric function of amorphous Ta_2O_5 is in excellent agreement with the data by Bright et al.[32] for the Drude and Lorentz part, and $\epsilon_\infty = 4.8$. The real part (ϵ_1) of the permittivity is shown in the upper panel in Figure 2a and the imaginary part (ϵ_2) in the lower panel, for the phononic contributions (grey), the Drude (black) contributions and the overall permittivity (blue). The phonon resonances manifest themselves as peaks in ϵ_2 and a derivative line shape in ϵ_1 (only minimum visible here). The Drude contribution here consists of the first two terms in Equation (1). The overall permittivity is dominated by the phononic contributions, while the

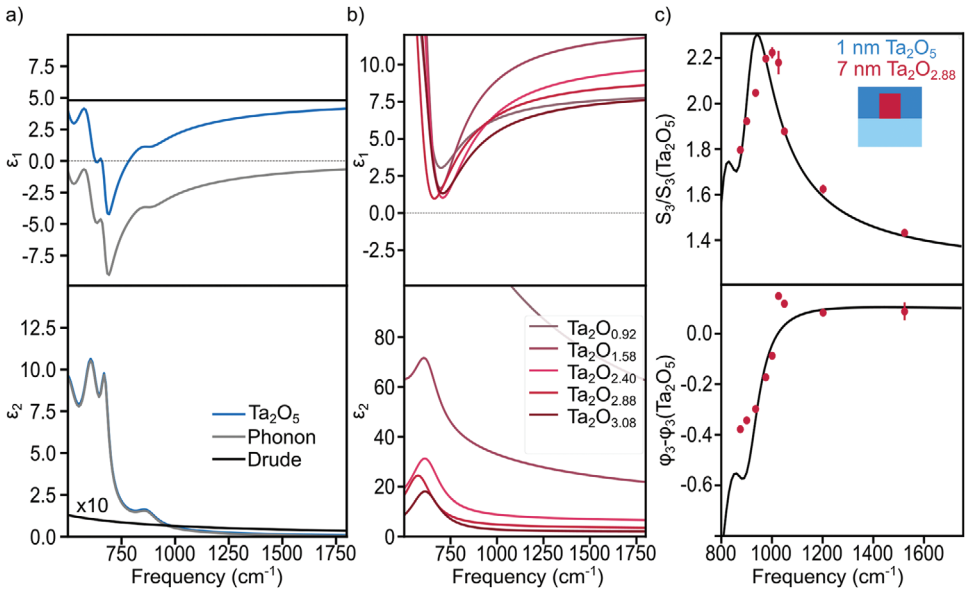

Figure 2. Optical response of a locally switched filament. a) Real (ϵ_1) and imaginary (ϵ_2) part of the permittivity of Ta_2O_5 (blue), and its individual contributions, the Phonon (grey), and the Drude (black). b) ϵ_1 and ϵ_2 extracted from oxygen-deficient samples via FTIR reflection measurements for different stoichiometries of Ta_2O_X (x = 3.08, 2.88, 2.4, 1.58, 0.92). c) s-SNOM amplitude and phase spectra from sequential s-SNOM spectroscopy of the filament shown in Figure 1e normalized to the adjacent Ta_2O_5 in comparison to finite dipole model (FDM) simulations for a filament of 1 nm Ta_2O_5 oxidation layer on top of 7 nm $Ta_2O_{2.88}$, as shown in the inset. Parameter sweep for different stoichiometries and film thicknesses is shown in Section S3, Supporting Information.

constant Drude contribution in ϵ_1 results in an offset of the total permittivity, while its contribution in ϵ_2 almost vanishes. This results in a phonon-like resonance with negative ϵ_1 for Ta_2O_5 around a minimum of the real part of the permittivity close to 750 cm^{-1}.

The obtained permittivities of the sub-stochiometric films are shown in Figure 2b (parameters in Section S2, Supporting Information). For the fits only a single phonon oscillator was assumed, as the higher damping in the Drude part suppresses the smaller phononic contributions at lower frequencies. In accordance with a damping of the phonon resonance, because of an increase in the damping of the Drude part γ_D, we can see an increasing ϵ_2 with decreasing oxygen content. With decreasing oxygen content, ϵ_1 is shifted to higher values and the zero crossing is absent. The increase of the damping results in a non-diverging real part of the Drude permittivity at low frequencies, accompanied by strong damping of the phonons, due to electron-phonon coupling because of the presence of charge carriers. Similar behavior has been observed for $Ge_3Sb_2Te_6$ phonons at very low frequencies[34] and $SrTiO_3$.[24]

Figure 2c compares the amplitude (S_3) and phase contrasts (ϕ_3) obtained from images at each frequency to theoretical simulated contrasts. The maximum amplitude at the spot was determined, by fitting a Gaussian curve to the spots and referencing the determined signal to the surrounding 8 nm Ta_2O_5 film. We calculate the expected s-SNOM contrast via the finite dipole model (FDM) for multilayer samples[35] (Section S3, Supporting Information), assuming laterally homogenous individual layers for a simplified description. We justify this assumption, with the filament's diameter (60 nm) being larger than the s-SNOM tip's diameter.

The exponentially decaying NF can be used in this model to investigate the vertical composition of the sample, by comparing theoretical simulated contrasts to our experimental data. The experiments were conducted under ambient conditions and no electrode protecting from oxidation is present. Thus, in the simulations we consider a passivation layer of Ta_2O_5 forming on top of the switched filament. The filament composition is estimated to be a 1–2 nm thick passivation layer of Ta_2O_5 and an oxygen-deficient part with a vertical extension of 7 ± 1 nm. The oxygen-deficient part has an optical response like a film with an oxygen content x between 2.40 and 2.88 (Ta_2O_x) (Section S3, Supporting Information). These calculations also show that even strong variations in the material stacking order do not significantly influence the result.

Stoichiometries in a similar range have been reported in XPEEM for filaments that cannot be switched anymore, so-called hard dielectric breakdowns, with a stoichiometry of x = 3.4 ± 0.2.[13] For this hard dielectric breakdown, the local oxygen vacancy concentration is so high that the resistive switching process is inhibited.[2,13] In the literature, there are reports for the stoichiometry of filaments in Ta_2O_5, varying between x = 2 for transport[8] and up to x = 4 in XPEEM,[13,14] aligning with the observations made here. Our findings suggest that sequential s-SNOM spectroscopy of a filament can determine its composition by comparing the s-SNOM response to dielectric properties of oxygen-deficient samples due to the sensitivity of infrared light to characteristic phonon and charge carrier contributions of the permittivity. In the future, more refined models for the permittivity $\epsilon(\nu)$ could take into account polaron effects[36] or different frequency-dependent damping for LO and TO modes and impurity modes.[33] Although, the current fit model has its limitations,

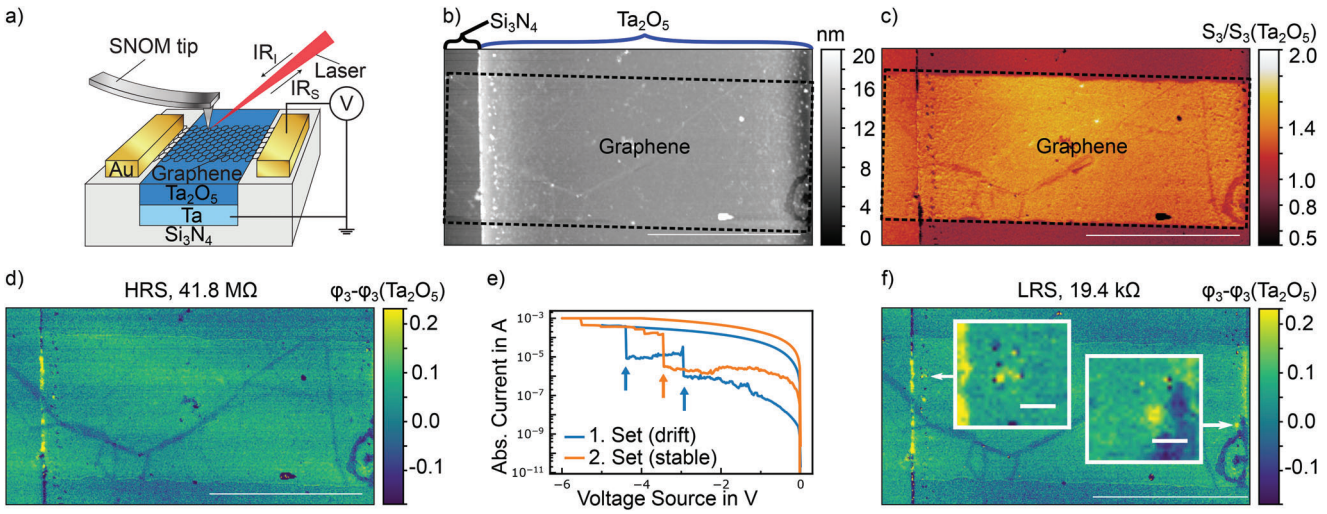

Figure 3. In situ switching and imaging of a device with a graphene top electrode. a) Sketch of a Ta_2O_5 device in crossbar architecture, consisting of a graphene top electrode, an 8 nm Ta_2O_5 active layer, and a bottom electrode of tantalum. Two gold leads contact the graphene top electrode. The bottom electrode is on ground potential. A voltage between the top and bottom electrodes is applied to form and switch the sample. b) AFM and c) third demodulation order (S_3) amplitude images (900 cm^{-1}) of a Ta_2O_5 thin film device. The Si_3N_4 substrate, the Ta_2O_5, and the graphene-covered area are highlighted. d) Corresponding phase image (ϕ_3) of the device. Note that the device was previously formed and switched and is in the HRS. e) Switching curves from the HRS to a stable LRS. Two switching steps were needed to achieve a stable LRS state. Arrows indicate jumps in the switching curves. f) ϕ_3 image of the device after the two switching cycles. During the switching, the graphene remained intact. Two new bright spots can be observed on the devices' left and right sides, indicated by the white arrows. The insets show a zoom-in (scale bar 200 nm). All other scale bars are 5 µm.

a physically meaningful explanation of the observed amplitude and phase data was achieved by the straightforward superposition of electronic and phononic contributions. Up to now, we have only discussed the composition of the layers. The spectroscopic results could be further improved by combining s-SNOM spectroscopy with model calculations taking into account exact filament shapes obtained by c-AFM tomography or TEM. For example, complementary measurements of s-SNOM and c-AFM tomography could be performed, as both methods can be applied to programmed devices, whose top electrode has been delaminated.

After showing the possibility of microscopy and spectroscopy with a single locally switched filament, we investigate devices with a graphene top electrode to observe the position and lateral distribution of filaments in these devices. Devices with a graphene top electrode have shown comparable switching behavior to Pt top electrode devices previously,[13] differing only by the addition of a series resistance introduced by the graphene. This allows for the transfer of findings on these devices to more standard ReRAM devices. The working principle of an s-SNOM measurement during device operation is depicted in **Figure 3a**. The device is fabricated in a crossbar architecture, consisting of an inert graphene top electrode instead of a metal top electrode, similar to the configuration used for PEEM measurements,[13,21] contacted by gold metal leads, and an Ohmic tantalum bottom electrode, which is grounded. The Ta_2O_5 film and the bottom electrode are embedded in a Si_3N_4 substrate. A voltage is applied between the top and bottom electrodes to form and switch the sample. Upon forming the device, at least one filament forms. The filament-forming position is randomly located on the electrode area at the active graphene/Ta_2O_5 interface. Subsequently, the device can be reversibly switched from the low resistive state (LRS) to the high resistive state (HRS) by applying an opposite voltage. The reported counter-eight-wise switching behavior of a device with a graphene top electrode is qualitatively similar to devices with a Pt top electrode.[13]

In Figure 3b, an AFM image of a device in the HRS with a resistivity of 41.8 MΩ is shown. From left to right, we can see the Si_3N_4 substrate and the Ta_2O_5 film. The black dashed box indicates the graphene-covered part of the substrate and Ta_2O_5 (active electrode). Close to the edge between the substrate and the Ta_2O_5 film, inhomogeneities can be observed, which show an increased topography compared to their surroundings. In Figure 3c, the simultaneously recorded s-SNOM amplitude image at 900 cm^{-1} is shown. The graphene lights up compared to the surrounding Ta_2O_5, making it much easier to identify the graphene-covered parts. The strong contrast of the graphene-covered Ta_2O_5 towards the surrounding graphene is caused by free charge carriers inside of the graphene that are excited resonantly at 900 cm^{-1} (s-SNOM contrast calculations shown in Section S4, Supporting Information). Here, the graphene mobility and charge carrier density are too low to support propagating surface plasmon polaritons which can be observed in higher quality samples at similar frequencies,[37,38] instead only the high s-SNOM amplitude signal can be observed. The graphene shows line-like defects (darker lines) all over the image and a minor half-circular defect at the bottom right. Figure 3d displays the corresponding third demodulation order phase image (ϕ_3) of the device. Similar features, as in (c), can be observed. However, the graphene electrode is much harder to identify in the phase images. Additionally, bright features can be observed at the left edge between the substrate and the Ta_2O_5 film. These features are defects that arise at the interfaces during the fabrication process of the device.

In Figure 3e, the *I–V* curves of two switching processes applied to the device from an HRS with 41.8 MΩ to the LRS are shown.

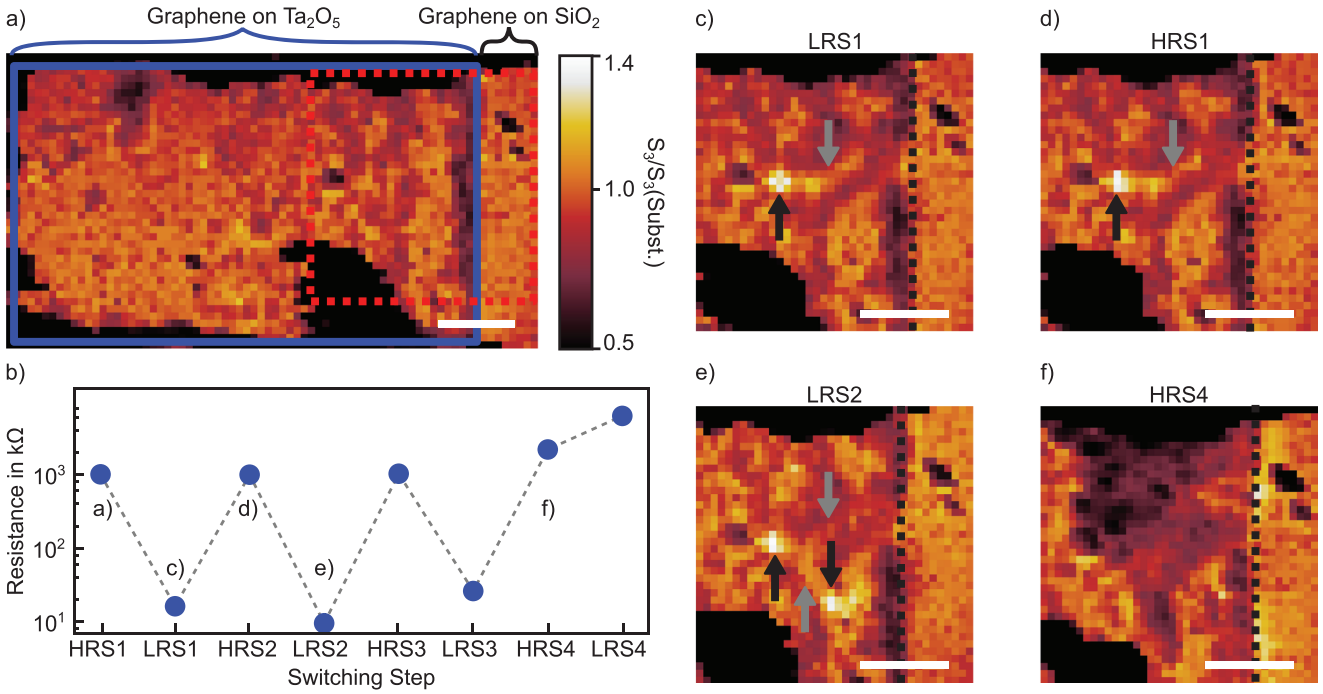

Figure 4. Tracking of a device over seven switching steps. a) s-SNOM amplitude (S_3) image of the active area in its initial state (HRS1) recorded at 1060 cm^{-1}. The red box in a) highlights the area of the images in (c–f). b) Resistance for each switching step of the device measured in-operando (resistances are read out at −0.2 V) between the s-SNOM measurements until failure in HRS4, switching curves in Section S5, Supporting Information. c–f) corresponding amplitude images of selected states. The black dotted line marks the boundary between the electrode area of Ta_2O_5 (left side) and substrate (right side). Black arrows mark the bright spots, and grey arrows mark the ridge-like feature. The scale bars correspond to 500 nm.

Two switching steps are needed. The first switching curve (blue) demonstrates two current jumps (blue arrows), one close to −3 V and the other close to −4.5 V, resulting in an initial low resistive state of 157 kΩ, gradually increasing to 575 kΩ. This atypically bad retention results from the graphene top electrode.[13] The device was switched a second time with a slightly higher voltage to stabilize a potential filament, resulting in a single jump (orange arrow) in the current. Subsequently, the resistance remained stable between 30 and 40 kΩ throughout the s-SNOM imaging of the device shown in Figure 3f, indicating that the device remained in the low resistive state (LRS) during the entire course of the measurement. In Figure 3f, the phase image after switching is shown, revealing two new bright spots near the edge of the device. White arrows indicate the positions of the spots. The insets highlight these two spots, revealing two changes in the device over the course of two switching events from (d) to (f).

The two spots appearing in the phase image in Figure 3f can be attributed, similarly to the previous results of the locally formed filament, to a local change in the permittivity. In combination with the switching of the devices from the HRS to the LRS state, as shown in Figure 3d, we attribute these two spots to be filaments. To further support this argument, we conducted additional s-SNOM contrast simulations for the available sub-stoichiometric permittivities that predict a pronounced phase contrast at 900 cm^{-1} with respect to the surrounding graphene (Figure S4, Supporting Information). In these simulations, the phase contrast decreases with increasing oxygen content. Here, we expect the oxygen content to be even higher than in the available sub-stoichiometries ($x < 3.1$) shown in Figure 2, as switchable filaments are present. The oxygen content of switchable filaments was determined in XPEEM to be $x = 4 \pm 0.1$ for Ta_2O_5.[13] Therefore, we expect a lower phase contrast than our s-SNOM contrast simulations suggested.

These results highlight, that s-SNOM is capable of imaging switchable filaments in ReRAM devices with a graphene top electrode non-invasively and allows for tracking of the filament morphology inside the device, despite the presence of a top electrode. No preferential forming of filaments at graphene defects such as folds and cracks has been found similar to previous work on this device type.[13]

A significant obstacle in the s-SNOM measurements of devices is the size of the active electrode area and the high resolution required to image the small filaments. Therefore, we turn to a smaller device which allows for much faster imaging and for the tracking of a device over seven switching steps. The device has a SiO_2 substrate. In **Figures 4** and **5**, the simultaneously recorded s-SNOM amplitude (S_3) and phase (ϕ_3) images, recorded after each switching step at a frequency of 1060 cm^{-1}, are shown. We chose 1060 cm^{-1}, as we expected both a strong amplitude contrast of a potential filament to the surrounding and a strong phase contrast of graphene-covered to non-covered Ta_2O_5 (contrast simulation, Section S4, Supporting Information). Our aim is to track the evolution of potential filaments and the active electrode simultaneously in each switching step with good visibility (signal-difference to noise ratio).

Figure 4a shows the third demodulation order amplitude (S_3) image of a device. The active electrode area, where the graphene is on top of the Ta_2O_5 is indicated by a blue box and marked by

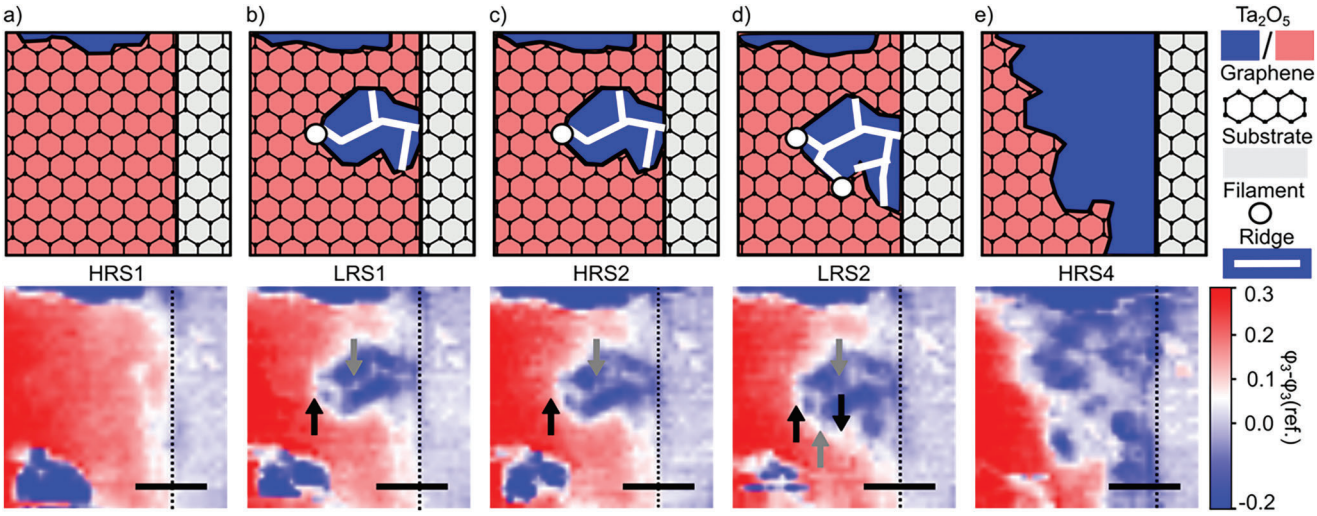

Figure 5. Retraction of graphene and rise of ridge-like features: Sketch (top row) and normalized s-SNOM phase (ϕ_3) image (bottom row) of the active area of the cell shown in Figure 4 in the different states recorded at 1060 cm^{-1}. The sketches highlight significant changes in the cell according to the amplitude and phase images: Retraction of the graphene and the rise of ridge-like features and filaments. The graphene-covered area is shown as a hexagonal lattice on top of the Ta_2O_5 (light red) and substrate. Bare Ta_2O_5 is shown as blue. In the bottom row, the vertical black dotted line marks the boundary between the electrode area (left side) and substrate (right side), black arrows indicate the filament position of Figure 4 and grey arrows indicate the ridge-like features observed in the amplitude images in Figure 4. The scale bars correspond to 500 nm.

the curly bracket. The graphene is on top of the surrounding SiO_2 substrate on the right side of the blue box. Via this area, the active electrode is connected to the metal leads (not shown in the images, see Figure 3). The graphene is electrically connected only on the right side to the lead, unlike Figure 3, where the graphene was connected on both sides. The device was switched by applying an external ramped voltage with a current compliance of 1 mA. We measured the device's resistance after each switching step via *I–V* curves at a read-out voltage of −0.2 eV and subsequently scanned it with s-SNOM. Figure 4b plots the measured resistance against the seven switching steps (switching curves in Figure S5, Supporting Information). Repeated switching resulted only in slight variations of the resistance in the HRS and LRS states, resulting in a reproducible switching behavior of the device for three cycles. For the HRS, states 1–3 resistances are ≈1 MΩ and vary within a range of 30 kΩ. The LRS states 1–3 varied in a narrow window between 9.5 and 26.1 kΩ, measured before imaging, and exhibited a drift in the resistance of less than 10 kΩ during imaging.

The graphene top electrode most likely limits the retention of the device, resulting in a resistance drift. Six switching steps were successful, with the device getting stuck in the HRS4 with a resistivity of 3.3 MΩ after the last step. Switching back to the LRS4 failed, even increasing the device's resistance. Although macroscopic resistance measurements showed similar resistances for HRS and LRS, individual switching steps caused significant changes to the device, as seen in the s-SNOM imaging of the area marked by the red dotted box. In Figure 4c–f, s-SNOM amplitude (S_3) images are shown after the switching steps LRS1, HRS2, LRS2, and the last successful switching step to HRS4. Figure 4c was recorded after switching the device from the high resistive state (initial, HRS1) to the first low resistive state (LRS1). A bright spot appears on the device, indicated by a black arrow. In accordance with our previous results and our s-SNOM response modeling (Section S4, Supporting Information), we identify the bright spot as a filament. Additionally, a ridge-like feature (grey arrow) appears right of the filament, almost entirely connecting it to the graphene-covered substrate on the right side. In Figure 4d, recorded after switching the device from the LRS1 to the HRS2 state, both the filament and the ridge remain, and there are no significant changes in the device. Subsequently, in Figure 4e, recorded after switching the device from HRS2 to LRS2, a second filament is visible on the device (2nd black arrow). Moreover, a second ridge forms (2nd grey arrow), connecting the two filaments. After the last successful switching step from LRS3 to HRS4 (Figure 4f), a large dark area appears in the s-SNOM amplitude image. Further analysis and discussion of the dark area can be found in the supporting information, as it corresponds to a pyramid-like structure in the AFM topography images (Section S6, Supporting Information), that arose after switching.

Through imaging the active electrode area of the device during seven switching steps, we were able to track the evolution of filaments through their strong optical contrasts. Despite changes in the topography, the optical contrasts remained dominant (Discussion, see Section S6, Supporting Information). While we can observe filaments in the device, we cannot distinguish them in terms of conductivity, solely by s-SNOM imaging so far. Thus, we could not differentiate between the HRS and LRS states because the change in the vertical filament composition is too small for the s-SNOM to detect the difference. Upon switching the oxygen vacancy-rich filament from the LRS to the HRS state, a disk of low oxygen vacancy concentration forms at the interface to the graphene. These discs are estimated to have a vertical height of less than two nanometers.[39] To detect such small changes in thickness and oxygen-vacancy concentration in the devices in the future, the sensitivity of s-SNOM can be further enhanced, for example, by resonant enhancement of the tip,[40] the use of different harmonics (2, 3, and 4 Ω) which have different probing volumes,[29] referencing to a film of similar thickness[41] or

recording of spectra of a single filament with a broadband IR light source (Nano-FTIR).[23]

In Figure 5, the corresponding third demodulation order phase images (ϕ_3) at the frequency of 1060 cm^{-1} and sketches highlighting the most significant features for each state, the extension of the graphene top electrode, the ridge-like features, and filaments are shown. At the frequency of 1060 cm^{-1} Ta_2O_5 areas covered by graphene show a strong phase contrast towards non-covered areas (see Section S4, Supporting Information). In Figure 5a, the Ta_2O_5 is almost entirely covered by graphene (hexagonal lattice + light red color in sketch). The phase values are above 0.1 rad in images where the graphene is above the Ta_2O_5 ("active electrode"), with a small blue area at the bottom left and top exhibiting phase values below −0.1 rad (blue). On the right side, the graphene is on top of the SiO_2 substrate, with a phase contrast around 0.05 rad (white blueish). Via the graphene-covered substrate, the active electrode is connected to the metal leads (not shown in the images). The graphene is only connected on the right side to the lead.

In Figure 5b, upon switching from HRS1 to LRS1, an additional blue area appears on the previously Ta_2O_5-covered areas with phase values below 0 rad. This indicates the retraction of graphene and subsequent revealing of the underlying Ta_2O_5. A ridge-like feature appears (white/blueish), marked by the grey arrow. This feature spans over the area of the missing graphene, from the position of the black arrow (corresponding to the filament in Figure 4c) to the graphene-covered substrate on the right side of the phase image. At the position of the black arrow, corresponding to the filament in Figure 4, no prominent feature can be identified. In Figure 5c, recorded after the subsequent switching of the device from the LRS1 to the HRS2 state, no significant changes occurred inside the device. In Figure 5d, recorded after switching the device from HRS2 to LRS2, the blue area increases. This indicates the further retraction of graphene. Furthermore, at two positions, ridge-like features appear. One is marked by the second grey arrow, right of the first black arrow, and appears to connect the two filaments. Another is close to the substrate. In Figure 5e, the phase image recorded after the last successful switching step from LRS3 to HRS4 is shown; the blue area extends now from the top to the bottom of the phase image. This indicates the full retraction of graphene connecting the top electrode to the substrate and, therefore a loss of electrical contact of the active electrode towards the metal leads. The loss of contact is also shown by the increased resistance in HRS4 and the failure to switch the device to the LRS again (Figure 4b). No contact between the top and bottom exists anymore, due to the retraction of the graphene. Thus, the subsequent retraction of the graphene electrode during the HRS to LRS switching steps finally led to the device's failure.

Each switching step, especially from the HRS to LRS, is accompanied by the retraction of graphene, as seen from the phase images in Figure 5. The graphene retracts due to local joule heating caused by high currents upon switching, as the power is dissipated within the conductive filament. This leads to oxidation and subsequent removal of the graphene from the surface. The retraction of the graphene stops as soon as the local temperature starts to fall, as at some point, the filament increases in size, additional filaments form, or the current compliance comes into effect (only after a few µs). In our case, Joule heating is expected, as we use current compliances of 1 mA and apply a bias of up to 7 V when switching to the LRS. The temperature in the filaments needs to increase to temperatures above 740 K, up to which graphene is stable in air.[42] During switching, temperatures of up to 1000 K are reported.[16,39,43] Here, the usage of multilayer graphene could result in slightly better lateral heat distribution, as shown for bilayer graphene compared to single-layer graphene.[16] The remaining connected filament needs to be at least partially covered by graphene to sustain an electrical contact as is the case here, sketched in Figure 5. The ridge-like features and the retraction of the graphene are two processes that go hand in hand. Upon retraction of the top electrode due to local joule heating, the filaments will follow the edge of the electrode sequentially in a path-like structure. A similar observation of the retraction of the top electrode (melting) and the following of the filaments due to local joule heating has been simulated and experimentally observed in Fe:$SrTiO_3$ devices, even with a metal top electrode.[44] Path-like structures have been reported for Ta_2O_5, namely the formation of dendrite-like structures by avalanche discharge between the top electrode and the reduced Ta_2O_x layer, which evolves at interface adsorbate layers,[14] most likely existing here due to wet-transferred graphene. These dendrites are essentially large filaments stretching over the devices and show an increased conductivity. However, determining whether the filaments follow the path sequentially or continuously from the s-SNOM measurements here is unattainable due to the resolution limit of the s-SNOM to 20 nm by the tip's radius. Thus, sequential growth of filaments with distances < 20 nm would result in an average signal that looks like a homogenous feature.

Following the ridge-like feature to its origin, the initial filament forms close to the defect-rich interface between the Ta_2O_5 and the substrate. Formation at the defects is preferred due to the increased presence of mobile donors.[1,6,45] A connection of a conductive path to the graphene-covered SiO_2 substrate can be excluded, as the switching of the device failed, after the full retraction of the top electrode.

3. Conclusion

Our experimental results reveal filaments in Ta_2O_5 thin films and oxide-based ReRAM devices by imaging with s-SNOM on the nanoscale with low-energy photons in the infrared spectral range. With this technique, we investigated the local spectroscopic response of a filament with 60 ± 5 nm diameter. We estimated its composition to be 7 ± 2 nm of Ta_2O_x with an oxygen content (x) between 2.4 and 2.88 and a native oxide layer on top of 2 nm, by comparing the s-SNOM's amplitude and phase data to theoretical s-SNOM spectra obtained from permittivity's of oxygen-deficient Ta_2O_x ($x < 5$) films.

We achieved imaging of filaments in devices with s-SNOM by replacing the typical metal top electrode with a graphene top electrode. These images revealed filaments in the devices upon switching and allowed us to trace filaments and changes within a device in operando over seven switching steps under ambient conditions. We revealed reproducible HRS and LRS states on the device level despite significant microscopic changes in the electrode material and the filament, such as retraction of the top electrode and formation of new filaments upon switching.

While s-SNOM performs worse than in situ TEM or c-AFM in terms of temporal and spatial resolution, we have shown several advantages of s-SNOM, such as the applicability to a lateral structure without delaminating the top electrode, the absence of special substrate preparation and the ease of application. Applying low-energy infrared photons (<0.2 eV) under ambient conditions allows for repeated in operando imaging of devices after individual switching steps. This opens the possibility for follow-up studies, such as live tracking of individual filaments by placing the tip on top of an individual filament and recording the scattering amplitude over time during the switching process. Further, our results pave the way for the investigation of the influence of illumination on the switching of oxides.[46,47]

Future studies involving s-SNOM would especially benefit from a smaller device layout. Nano-FTIR Spectroscopy[23] over a broad range in combination with further refined s-SNOM response modeling, could give deeper insights into the composition of the filament, especially determining the charge carrier density and mobility and the individual phonon parameters.

Our results establish s-SNOM as a tool for investigating filaments and defects in ReRAM devices, among other techniques such as PEEM, TEM, and c-AFM. Applying s-SNOM imaging and spectroscopy to oxide-based ReRAM devices has so far not been performed. However, it promises great potential as it is a tabletop solution for the investigation of memristive devices, and the technique is applicable to almost all metal and non-metal oxides, for example, SiO_2,[48,49] $SrTiO_3$,[24,50] Al_2O_3, TiO_2,[51] MoO_3,[52] ZrO, HfO_2, etc., regardless if the film is amorphous or crystalline. It is even applicable to oxide heterostructures such as layered $SrTiO_3/LaAlO_3$.[25,26]

4. Experimental Section

Thin Film Fabrication: The reference films of varying Ta_2O_x stoichiometry were prepared using reactive RF-sputtering employing different reactive gas flow rates, deposition rates, and oxygen concentrations in the process gas mixture. A more comprehensive description of the process parameters can be found in the Supporting Information of reference.[13]

Device Fabrication: Two different substrates were employed in this work. For the initial device shown in Figure 3, Si_3N_4 substrates were used, while the sample shown in Figure 4 was fabricated on a SiO_2 substrate.

Initially, the embedded Ta/Ta_2O_5 structures were fabricated by defining the structure of the bottom electrode in optical lithography, then using Ar ion beam etching for SiO_2 or CF_4 reactive ion beam etching for Si_3N_4 to etch a 40 nm deep trench. This trench was then filled by successively depositing 33 nm of Ta and 8 nm of Ta_2O_5 via reactive RF sputtering. After stripping the photoresist, commercial-grade, single-layer graphene (Graphenea, Spain) was deposited onto the sample. The process is described in more detail in the supporting information (Section S7, Supporting Information). A second optical lithography process in conjunction with oxygen plasma etching was used to structure the graphene into $10 \times 5\ \mu m^2$ pads. Finally, a third optical lithography process was employed to define contact leads of 10 nm Pt and 60 nm Au that were deposited via electron beam evaporation.

Electrical Characterization: *I–V* sweeps were performed using a Keithley 2611A SourceMeter. All voltages were applied to the top electrode for crossbar devices or to the tungsten needle for the forming induced in a homogeneous layer. For all sweeps, a hold time of 5 ms and a step width of 20 mV were chosen. Current compliances were noted explicitly when applied.

s-SNOM: A commercially available s-SNOM (NeaSNOM, neaspecGmbH) was used in combination with LN2-cooled MCT detectors (InfraredAssociates & Kolmar technologies). The s-SNOM was operated in pseudo-heterodyne detection mode, to record amplitude and phase simultaneously. The laser source was a commercially available MIRcat QCL by daylight solution. The s-SNOM was operated at tapping frequencies of 220–270 kHz at tapping amplitudes of 50 nm for the spectroscopy and 120 nm for the imaging of the device in Figures 4 and 5. The signal from the third demodulation order amplitude (S_3) and phase (ϕ_3) were extracted. The s-SNOM contrasts and the uncertainties evaluated in Figure 2c were determined by averaging the near-field amplitude and phase signals for the forward and backward scanning directions.

c-AFM: All c-AFM measurements were performed at a Cypher AFM (Asylum Research, USA) in contact mode. The sample was grounded using Al-wire bonding to the ground sample holder, and a bias of 2 V was applied via a Pt/Ir-coated cantilever.

Laser Cutting: The graphene top electrodes were patterned using a supercontinuum laser (NKT compact) coupled into an optical microscope setup. The setup allowed the translation of the sample by motorized stages and a gamepad controller, as well as live sample imaging while the laser was on.

The laser was operated at a repetition rate of 4 kHz and was filtered to a spectral range between 400 and 550 nm. The pulse duration on the sample was estimated to be a few tens of picoseconds. The power was varied using absorption filters.

FTIR: The FTIR spectroscopy data were collected using a Bruker Vertex 70 interferometer in conjunction with the motorized angle-variable reflection unit Bruker A513/Q in p-polarization. Specular reflection under the angles 13°, 25°, and 45° was measured for each Ta_2O_x film sample and referenced to reflection on optically thick gold and the same respective angles. For each spectrum, 100 scans were taken with a resolution of 16 cm^{-1} wavenumbers. The permittivity was then extracted by fitting a Lorentz model with multiple resonators (see main text and Section S2, Supporting Information).

Supporting Information

Supporting Information is available from the Wiley Online Library or from the author.

Acknowledgements

K.G.W. and K.G. contributed equally to this work. K.G.W., K.G., T.H., R.D., and T.T. conceived the research idea; K.G. and T.H. fabricated the samples and conducted the electrical switching; K.G.W. and C.B. conducted the s-SNOM measurements; A.H. conducted the FTIR measurements and the fitting; K.G.W., C.B., and H.L. analyzed the data and carried out the numerical simulations; L.W. cut the graphene top electrode; All authors contributed to writing the manuscript. This work was supported by the Excellence Initiative of the German federal and state governments, the Ministry of Innovation of North Rhine-Westphalia, and the Deutsche Forschungsgemeinschaft. K.G.W., K.G., T.H., A.H., R.D., and T.T. acknowledge support from the Deutsche Forschungsgemeinschaft (DFG) within the collaborative research center SFB917.

Open access funding enabled and organized by Projekt DEAL.

Conflict of Interest

The authors declare no conflict of interest.

Data Availability Statement

The data that support the findings of this study are available from the corresponding author upon reasonable request.

Keywords

filaments, memristive devices, near-field optical microscopy, tantalum oxide

Received: October 20, 2023
Revised: November 28, 2023
Published online: January 4, 2024

[1] R. Waser, R. Dittmann, G. Staikov, K. Szot, *Adv. Mater.* **2009**, *21*, 2632.
[2] H.-S. P. Wong, H.-Y. Lee, S. Yu, Y.-S. Chen, Y. Wu, P.-S. Chen, B. Lee, F. T. Chen, M.-J. Tsai, *Proc. IEEE* **2012**, *100*, 1951.
[3] A. J. Lohn, J. E. Stevens, P. R. Mickel, D. R. Hughart, M. J. Marinella, *ECS Trans.* **2013**, *58*, 59.
[4] M.-J. Lee, C. B. Lee, D. Lee, S. R. Lee, M. Chang, J. H. Hur, Y.-B. Kim, C.-J. Kim, D. H. Seo, S. Seo, U.-I. Chung, I.-K. Yoo, K. Kim, *Nat. Mater.* **2011**, *10*, 625.
[5] C. Funck, S. Menzel, *ACS Appl. Electron. Mater.* **2021**, *3*, 3674.
[6] R. Dittmann, S. Menzel, R. Waser, *Adv. Phys.* **2021**, *70*, 155.
[7] F. Miao, J. P. Strachan, J. J. Yang, M.-X. Zhang, I. Goldfarb, A. C. Torrezan, P. Eschbach, R. D. Kelley, G. Medeiros-Ribeiro, R. S. Williams, *Adv. Mater.* **2011**, *23*, 5633.
[8] C. M. M. Rosário, B. Thöner, A. Schönhals, S. Menzel, M. Wuttig, R. Waser, N. A. Sobolev, D. J. Wouters, *Appl. Phys. Lett.* **2018**, *112*, 213504.
[9] C. Baeumer, R. Valenta, C. Schmitz, A. Locatelli, T. O. Mentes, S. P. Rogers, A. Sala, N. Raab, S. Nemsak, M. Shim, C. M. Schneider, S. Menzel, R. Waser, R. Dittmann, *ACS Nano* **2017**, *11*, 6921.
[10] C. Bengel, A. Siemon, F. Cuppers, S. Hoffmann-Eifert, A. Hardtdegen, M. Von Witzleben, L. Hellmich, R. Waser, S. Menzel, *IEEE Trans. Circuits Syst. I* **2020**, *67*, 4618.
[11] F. Miao, W. Yi, I. Goldfarb, J. J. Yang, M.-X. Zhang, M. D. Pickett, J. P. Strachan, G. Medeiros-Ribeiro, R. S. Williams, *ACS Nano* **2012**, *6*, 2312.
[12] G.-S. Park, Y. B. Kim, S. Y. Park, X. S. Li, S. Heo, M.-J. Lee, M. Chang, J. H. Kwon, M. Kim, U.-I. Chung, R. Dittmann, R. Waser, K. Kim, *Nat. Commun.* **2013**, *4*, 2382.
[13] T. Heisig, K. Lange, A. Gutsche, K. T. Goß, S. Hambsch, A. Locatelli, T. O. Mentes, F. Genuzio, S. Menzel, R. Dittmann, *Adv. Electron. Mater.* **2022**, *8*, 2100936.
[14] K. Skaja, C. Bäumer, O. Peters, S. Menzel, M. Moors, H. Du, M. Bornhöfft, C. Schmitz, V. Feyer, C.-L. Jia, C. M. Schneider, J. Mayer, R. Waser, R. Dittmann, *Adv. Funct. Mater.* **2015**, *25*, 7154.
[15] A. Wedig, M. Luebben, D.-Y. Cho, M. Moors, K. Skaja, V. Rana, T. Hasegawa, K. K. Adepalli, B. Yildiz, R. Waser, I. Valov, *Nat. Nanotechnol.* **2016**, *11*, 67.
[16] S. Deshmukh, M. M. Rojo, E. Yalon, S. Vaziri, C. Koroglu, R. Islam, R. A. Iglesias, K. Saraswat, E. Pop, *Sci. Adv.* **2022**, *8*, abk1514.
[17] T. Swoboda, X. Gao, C. M. M. Rosário, F. Hui, K. Zhu, Y. Yuan, S. Deshmukh, Ç. Köroglu, E. Pop, M. Lanza, H. Hilgenkamp, M. M. Rojo, *ACS Appl. Electron. Mater.* **2023**, *5*, 5025.
[18] U. Celano, L. Goux, A. Belmonte, K. Opsomer, A. Franquet, A. Schulze, C. Detavernier, O. Richard, H. Bender, M. Jurczak, W. Vandervorst, *Nano Lett.* **2014**, *14*, 2401.
[19] M. Buckwell, L. Montesi, S. Hudziak, A. Mehonic, A. J. Kenyon, *Nanoscale* **2015**, *7*, 18030.
[20] W. Sun, B. Gao, M. Chi, Q. Xia, J. J. Yang, H. Qian, H. Wu, *Nat. Commun.* **2019**, *10*, 3453.
[21] C. Baeumer, C. Schmitz, A. Marchewka, D. N. Mueller, R. Valenta, J. Hackl, N. Raab, S. P. Rogers, M. I. Khan, S. Nemsak, M. Shim, S. Menzel, C. M. Schneider, R. Waser, R. Dittmann, *Nat. Commun.* **2016**, *7*, 12398.
[22] G. Di Martino, A. Demetriadou, W. Li, D. Kos, B. Zhu, X. Wang, B. De Nijs, H. Wang, J. Macmanus-Driscoll, J. J. Baumberg, *Nat. Electron.* **2020**, *3*, 687.
[23] F. Huth, A. Govyadinov, S. Amarie, W. Nuansing, F. Keilmann, R. Hillenbrand, *Nano Lett.* **2012**, *12*, 3973.
[24] M. Lewin, C. Baeumer, F. Gunkel, A. Schwedt, F. Gaussmann, J. Wueppen, P. Meuffels, B. Jungbluth, J. Mayer, R. Dittmann, R. Waser, T. Taubner, *Adv. Funct. Mater.* **2018**, *28*, 1802834.
[25] W. Luo, M. Boselli, J.-M. Poumirol, I. Ardizzone, J. Teyssier, D. Van Der Marel, S. Gariglio, J.-M. Triscone, A. B. Kuzmenko, *Nat. Commun.* **2019**, *10*, 2774.
[26] J. Barnett, M.-A. Rose, G. Ulrich, M. Lewin, B. Kästner, A. Hoehl, R. Dittmann, F. Gunkel, T. Taubner, *Adv. Funct. Mater.* **2020**, *30*, 2004767.
[27] T. Taubner, R. Hillenbrand, F. Keilmann, *J Microsc* **2003**, *210*, 311.
[28] M. Lewin, B. Hauer, M. Bornhöfft, L. Jung, J. Benke, A.-K. U. Michel, J. Mayer, M. Wuttig, T. Taubner, *Appl. Phys. Lett.* **2015**, *107*, 151902.
[29] L. Mester, A. A. Govyadinov, S. Chen, M. Goikoetxea, R. Hillenbrand, *Nat. Commun.* **2020**, *11*, 3359.
[30] N. Ocelic, A. Huber, R. Hillenbrand, *Appl. Phys. Lett.* **2006**, *89*, 101124.
[31] Y. Ma, D. Li, A. A. Herzing, D. A. Cullen, B. T. Sneed, K. L. More, N. T. Nuhfer, J. A. Bain, M. Skowronski, *ACS Appl. Mater. Interfaces* **2018**, *10*, 23187.
[32] T. J. Bright, J. I. Watjen, Z. M. Zhang, C. Muratore, A. A. Voevodin, D. I. Koukis, D. B. Tanner, D. J. Arenas, *J. Appl. Phys.* **2013**, *114*, 083515.
[33] E. Franke, C. L. Trimble, M. J. Devries, J. A. Woollam, M. Schubert, F. Frost, *J. Appl. Phys.* **2000**, *88*, 5166.
[34] J. Barnett, L. Wehmeier, A. Heßler, M. Lewin, J. Pries, M. Wuttig, J. M. Klopf, S. C. Kehr, L. M. Eng, T. Taubner, *Nano Lett.* **2021**, *21*, 9012.
[35] B. Hauer, A. P. Engelhardt, T. Taubner, *Opt. Express* **2012**, *20*, 13173.
[36] G. D. Mahan, *Science* **1967**, *155*, 991.
[37] J. Chen, M. Badioli, P. Alonso-González, S. Thongrattanasiri, F. Huth, J. Osmond, M. Spasenovic, A. Centeno, A. Pesquera, P. Godignon, A. Zurutuza Elorza, N. Camara, F. J. G. De Abajo, R. Hillenbrand, F. H. L. Koppens, *Nature* **2012**, *487*, 77.
[38] Z. Fei, A. S. Rodin, G. O. Andreev, W. Bao, A. S. Mcleod, M. Wagner, L. M. Zhang, Z. Zhao, M. Thiemens, G. Dominguez, M. M. Fogler, A. H. C. Neto, C. N. Lau, F. Keilmann, D. N. Basov, *Nature* **2012**, *487*, 82.
[39] M. Von Witzleben, K. Fleck, C. Funck, B. Baumkötter, M. Zuric, A. Idt, T. Breuer, R. Waser, U. Böttger, S. Menzel, *Adv. Electron. Mater.* **2017**, *3*, 1700294.
[40] J. Aizpurua, T. Taubner, F. J. García De Abajo, M. Brehm, R. Hillenbrand, *Opt. Express* **2008**, *16*, 1529.
[41] K. G. Wirth, J. B. Hauck, A. Rothstein, H. Kyoseva, D. Siebenkotten, L. Conrads, L. Klebl, A. Fischer, B. Beschoten, C. Stampfer, D. M. Kennes, L. Waldecker, T. Taubner, *ACS Nano* **2022**, *16*, 16617.
[42] H. Y. Nan, Z. H. Ni, J. Wang, Z. Zafar, Z. X. Shi, Y. Y. Wang, *J. Raman Spectrosc.* **2013**, *44*, 1018.
[43] Y. Meng Lu, M. Noman, Y. N. Picard, J. A. Bain, P. A. Salvador, M. Skowronski, *J. Appl. Phys.* **2013**, *113*, 163703.
[44] C. Lenser, M. Patt, S. Menzel, A. Köhl, C. Wiemann, C. M. Schneider, R. Waser, R. Dittmann, *Adv. Funct. Mater.* **2014**, *24*, 4466.
[45] F. V. E. Hensling, H. Du, N. Raab, C.-L. Jia, J. Mayer, R. Dittmann, *APL Mater.* **2019**, *7*, 101127.
[46] M. E. Pereira, R. Martins, E. Fortunato, P. Barquinha, A. Kiazadeh, *Neuromorph. Comput. Eng.* **2023**, *3*, 022002.

[47] L. Hu, J. Yang, J. Wang, P. Cheng, L. O. Chua, F. Zhuge, *Adv. Funct. Mater.* **2021**, *31*, 2005582.
[48] M. B. Raschke, C. Lienau, *Appl. Phys. Lett.* **2003**, *83*, 5089.
[49] P. Li, X. Yang, T. W. W. Maß, J. Hanss, M. Lewin, A.-K. U. Michel, M. Wuttig, T. Taubner, *Nat. Mater.* **2016**, *15*, 870.
[50] J. Barnett, D. Wendland, M. Lewin, K. G. Wirth, A. Heßler, T. Taubner, *Appl. Phys. Lett.* **2022**, *120*, 211107.
[51] T.-X. Qin, E.-M. You, J.-Y. Zhang, H.-L. Wang, K. H. L. Zhang, B.-W. Mao, Z.-Q. Tian, *Nano Lett.* **2022**, *22*, 2755.
[52] W. Ma, P. Alonso-González, S. Li, A. Y. Nikitin, J. Yuan, J. Martín-Sánchez, J. Taboada-Gutiérrez, I. Amenabar, P. Li, S. Vélez, C. Tollan, Z. Dai, Y. Zhang, S. Sriram, K. Kalantar-Zadeh, S.-T. Lee, R. Hillenbrand, Q. Bao, *Nature* **2018**, *562*, 557.